

Received 17 July 2024, accepted 4 September 2024, date of publication 9 September 2024, date of current version 18 September 2024.

Digital Object Identifier 10.1109/ACCESS.2024.3456238



RESEARCH ARTICLE

Design, Implementation, and Control of a Ball-Balancing Robot

SANGSIN PARK[✉]

Department of Mechanical Engineering, Korea National University of Transportation, Chungju-si 27469, South Korea

e-mail: spark@ut.ac.kr

This work was supported by Korea National University of Transportation Industry-Academic Cooperation Foundation, in 2022.

ABSTRACT This paper presents the design, implementation, and control of a ball-balancing robot developed for interactive applications in service and entertainment environments. The robot features a unique thin and narrow body design to facilitate future functional expansions and a customized stepped planetary gear for the actuators, improving torque and precision. A compensator incorporating an observer and full-state feedback is developed and experimentally validated, ensuring accurate and stable control of the robot. Future work will focus on enhancing the stability and control mechanisms to improve the robot's performance in various applications.

INDEX TERMS Ball-balancing robot, customized stepped planetary gear, compensator.

I. INTRODUCTION

The field of robotics has seen significant strides since its early days, with innovations transforming how robots are utilized across various industries. One area that has particularly benefited from these innovations is the service and entertainment industry. From the simple, repetitive motions of early mechanical automatons to today's sophisticated robots capable of dynamic interactions with humans, the progress has been extraordinary. Robots have become integral to theme parks, restaurants, and even live performances, offering new forms of engagement and immersive experiences. Innovations in artificial intelligence and sensor technology have enabled robots to perform complex tasks, respond to human emotions, and navigate through intricate environments, significantly enhancing their role in the service and entertainment industry.

One of the robots in this field is the ball-balancing robot (BBR), a marvel of modern engineering and control systems. These robots, which balance on a single spherical wheel, provide unique advantages in maneuverability and interaction. Their ability to move smoothly in any direction without turning makes them ideal for dynamic and crowded environments such as theme parks, museums, and live events. BBRs can perform various entertaining tasks, from guiding

The associate editor coordinating the review of this manuscript and approving it for publication was Agustín Leobardo Herrera-May[✉].

visitors and delivering interactive performances to serving as mobile information kiosks. Their agility and responsiveness make them not only functional but also engaging and entertaining, capturing the imagination of audiences and pushing the boundaries of robotic entertainment. As these robots continue to advance, their role in the service and entertainment industry is expected to grow, offering even more innovative and captivating experiences.

An example of research relating a BBR is the study by Lauwers et al. [1], which presents a dynamically stable single-wheeled robot designed for omnidirectional movement, which balances on a spherical wheel using an inverse mouse-ball drive mechanism. The control system, combining a Proportional-Integral (PI) inner loop and an Linear Quadratic Regulator (LQR) outer loop, effectively maintains balance but struggles with precise trajectory tracking due to unmodeled frictional forces. The continuous research is the work by Nagarajan et al. [2]. They focus on a BBR with a four-motor inverse mouse-ball drive and a yaw drive mechanism for unlimited rotation about its vertical axis. They introduce a trajectory planning algorithm for smooth motion, validated through extensive experiments that showcase the robot's ability to handle disturbances and perform precise movements. The robot's design and control innovations highlight its potential for human interaction and dynamic navigation, making it a valuable asset in entertainment environments. Moreover, Nagarajan and Hollis [3] introduce

shape-accelerated balancing systems, a type of underactuated system where shape configurations map to accelerations in position space, exemplified by balancing mobile robots like the ballbot. Additionally, Seyfarth et al. [4] present SIMbot, a ballbot driven by a spherical induction motor (SIM), which simplifies the mechanical complexity of traditional ball-bal robots by reducing the number of active moving parts to just two—the body and the ball. Experimental results demonstrate SIMbot's effective balancing, station-keeping, precise point-to-point motion, and recovery from initial lean angles.

The study by Kumagai and Ochiai [5], [6] presents the development and control of a BBR. This research highlights the innovative design and engineering solutions implemented to achieve dynamic stability and precise maneuverability.

Another study is the work by Hertig et al. [7]. For a comprehensive approach to state estimation for a BBR, they propose a method that employs an Extended Kalman Filter (EKF) to fuse sensory information from incremental encoders, gyroscopes, and accelerometers. Unlike previous methods that separate attitude and position estimation, this unified approach allows for information flow in both directions, enhancing the overall accuracy of state estimates.

The study by Pham et al. [8] delves into the innovative design and control mechanisms of a human rideable BBR. They design the robot with a dynamic stability mechanism and implement the control strategy such as a double-loop approach, combining a PI inner loop for immediate control and a LQR outer loop for overall stability and trajectory tracking. The paper highlights the practical applications of the ball segway in environments requiring high agility and stability, such as human riding scenarios. This research significantly contributes to the field by presenting a comprehensive control strategy and validating it with real-world experiments. Moreover, the research by Pham et al. [9] address the complex challenge of synchronizing the motion between the ball and the body of the BBR to maintain equilibrium and achieve precise trajectory tracking. They propose a synchronization controller (SC) design that incorporates synchronization and coupling errors, and they apply this method to a dynamic model of the BBR. They validate their approach through extensive simulations and real-world experiments. The results demonstrate that the SC method offers stabilization accuracy and robust performance in both balancing and tracking tasks, even in the presence of external disturbances.

Jo and Oh [10] address the challenge of balancing and tracking control for a BBR by considering the contact forces between the robot and the ball. They propose a control framework that utilizes a projected task space dynamics approach with quadratic programming to handle inequality constraints such as friction and unilateral constraints. By dividing the task space dynamics into separate dynamics for the robot and the ball, the control input can be derived more effectively through the ball task dynamics. This decomposition allows for optimal contact force computation, which is crucial for maintaining balance and accurate trajectory tracking.

Lee and Park [11] introduce a virtual angle-based sliding mode control method to address the challenges of underactuation and nonlinear dynamics inherent in a BBR. This method uses a single-loop controller to achieve both trajectory tracking and balancing, simplifying the control system and enhancing robustness against external disturbances and model uncertainties.

Xiao et al. [12] design a BBR capable of carrying heavy loads. They develop a cascaded LQR-PI controller to address the drivetrain's nonlinear dynamics and high stiction issues. This controller combines an outer LQR loop for optimal trajectory generation with an inner PI loop for precise tracking and friction compensation.

The work by Jang et al. [13] presents a control method for a BBR. This method combines a virtual angle-based control strategy with an adaptive observer using radial basis function neural networks to estimate velocity information, thereby eliminating the need for direct velocity measurements. The proposed control system addresses the challenges of underactuation and nonlinearities in a BBR, ensuring the convergence of tracking and balancing errors without the local minimum problems associated with hierarchical control methods.

Fankhauser and Gwerder [14] proposes a comprehensive three-dimensional model to improve upon the limitations of current planar decomposition methods. Real-time simulations with a gain-scheduled controller demonstrate significant improvements, enabling the ballbot to follow complex trajectories with enhanced performance and robustness.

Lal et al. [15] introduce the development of a BBR and the design of its controller. The modular design facilitates future expansions and adjustments. Real-time control tests using a linear quadratic regulator show effective performance.

The study by Inal et al. [16] introduces fully-coupled 3D dynamic model for spherical wheeled self-balancing robots, which addresses limitations of previous 2.5D models by capturing important aspects such as yaw dynamics and coupled inertial effects. The simulations show that the 3D model can accurately track desired trajectories and handle complex motions, highlighting its advantages over simpler models.

Endo and Nakamura [17] develop the “B.B. Rider” (Basketball Rider) robot, which human can ride. The robot uses a basketball as a low-cost and effective spherical tire, incorporating orthogonal wheels and a six-axis force-torque sensor to enable movement and balance.

My contributions to the BBR include the development of a unique thin and narrow body design to enable functional expansion for future BBRs, the design of a customized stepped planetary gear for the actuators, and the experimental validation of the new design using a compensator composed of an observer and full-state feedback.

The paper is organized as follows. Section II provides the development of the BBR including details of the actuator and electronic parts. The mathematical model of the BBR is described in Section III and a balancing control scheme is

presented in Section IV. In Sections V, experiment results are presented. Finally, discussion and conclusions are described in Sections VI and VII, respectively.

II. DEVELOPMENT OF A BALL-BALANCING ROBOT

The aims of the robot's design are to interact with humans in service areas and to assist at live events. Thus, I have developed a ball-balancing robot (BBR) with a mass of 8.9 kg, a height of 90 cm, and a thin body with a diameter of 14.5 cm. A rendering of the BBR is presented in Fig. 1. The following provides a detailed description.

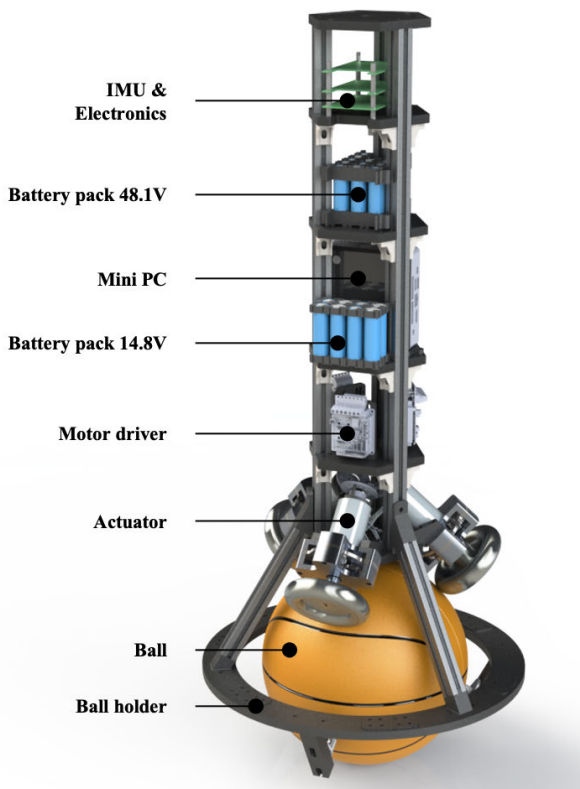


FIGURE 1. A rendering of a designed ball-balancing robot.

A. AN ACTUATOR

Three actuators are needed to rotate the ball. Each actuator consists of an omniwheel, a customized stepped planetary gear, a brushless DC (BLDC) motor, and a magnetic encoder. An exploded view of the actuator is shown in Fig. 2. The diameter of the omniwheel is 100 mm. The BLDC motor used is the Maxon EC-i 40 100W motor, and the motor driver is the Elmo Gold Solo Whistle. A magnetic encoder by RENISHAW is used to measure the omniwheel's angular velocity.

Regarding the customized planetary gear, a sectional view of the gear is presented in Fig. 3. This design can be used to achieve high gear ratios while maintaining a compact and efficient form factor. The features of this gear are as follows. The sun gear, which serves as the input, is connected to the

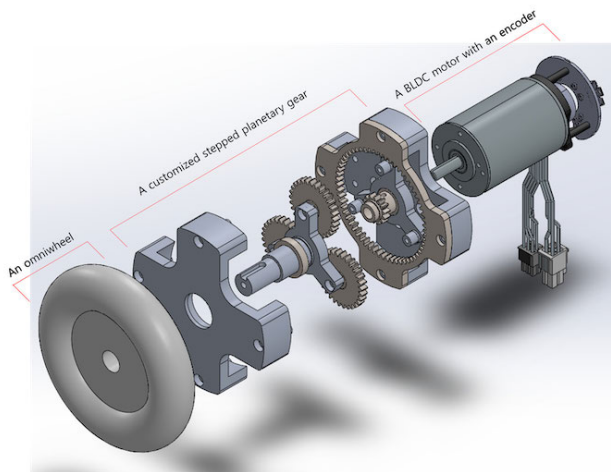


FIGURE 2. An exploded view of the actuator.

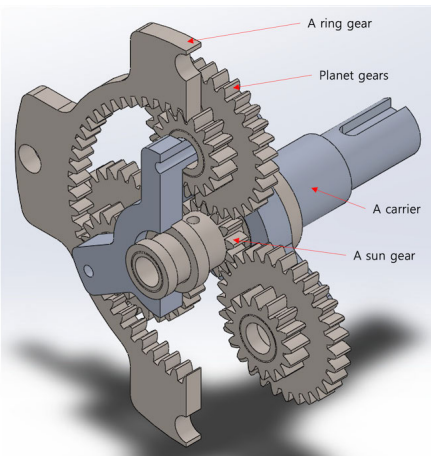


FIGURE 3. A sectional view of a customized stepped planetary gear.

motor shaft and drives the planetary gears. The ring gear is fixed in place, while the carrier, which serves as the output, is connected to the omniwheel. Each planet gear is composed of two different gears that rotate around the sun gear, and provides two stages of gear reduction. Thus, its primary advantage is the ability to provide higher gear ratios within a smaller space compared to a single-stage planetary gear. To calculate the gear ratio of that planetary gear system where the sun gear is the input and the carrier is the output with the ring gear fixed, the relationship is derived as follows.

$$\left| \frac{\omega_r - \omega_c}{\omega_s - \omega_c} \right| = \frac{N_{driving}}{N_{driven}}, \quad (1)$$

where ω_s , ω_r , ω_c , $N_{driving}$, and N_{driven} are the angular velocities of sun gear, ring gear, and carrier, product of the number of teeth on the driving gears, and product of the number of teeth on the driven gears, respectively. Rewriting (2),

$$\frac{\omega_r - \omega_c}{\omega_s - \omega_c} = - \frac{N_{p_2} N_s}{N_r N_{p_1}} = -K, \quad (2)$$

where N_s , N_r , N_{p_1} , and N_{p_2} are the numbers of teeth on the sun, ring, first stage planet, and second stage planet gears, respectively. Rearranging (2),

$$\omega_r = (1 + K)\omega_c - K\omega_s. \quad (3)$$

The left side of (3) is $\omega_r = 0$ because the ring gear is fixed. Thus,

$$\begin{aligned} \omega_c &= \frac{K}{1 + K}\omega_s \\ &= \frac{N_{p_2}N_s}{N_rN_{p_1} + N_{p_2}N_s}\omega_s \end{aligned} \quad (4)$$

The sun, ring, and planet gears are designed with a module of 1.0. In addition, the number of teeth on the sun and ring gears are 7 and 30, respectively. For the planet gears, the number of teeth on the first and second stages are 15 and 8, respectively. From (4), the gear ratio of the customized stepped planetary gear is 9.0357:1.

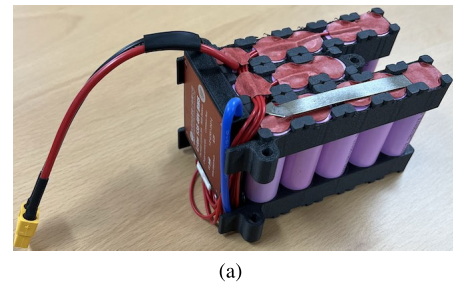
B. BATTERY PACKS AND AN INTERFACE MODULE

To separate the PC power source from the power source for the motor drivers, I fabricated two battery packs using 18650 Li-Ion batteries with battery management systems, which are shown in Fig. 4. The 13S1P battery pack (33.15Ah) consists of 13 cells connected in series, with a nominal voltage of 48.1V and a charging voltage of 54.6V. This battery pack is used as the power source for driving the BLDC motor and operating the microcontroller and an inertial measurement unit (IMU). The 4S2P battery pack (28Ah) consists of two sets of 4 cells connected in series, which are then connected in parallel. It has a nominal voltage of 14.8V and a charging voltage of 16.8V. This battery pack is used as the power source for operating the mini PC. The capacity of the two batteries is sufficient to operate the robot hardware and PC for around 1 hour.

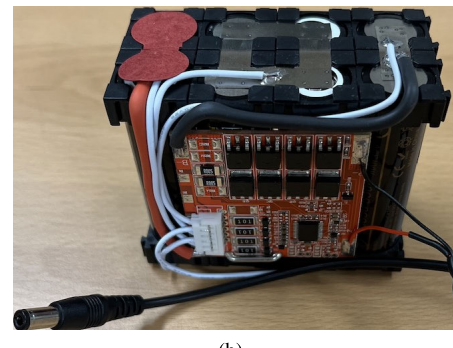
The interface module consists of three stacked PCBs. The bottom PCB has two DC-DC converters that converts 48V to 12V and 5V. The second layer PCB is an STM32F413VGT microcontroller PCB used for acquiring IMU sensor values. The top PCB is where the IMU sensor and connectors are mounted.

C. FABRICATION

In Fig. 6, the actual assembled BBR is shown and the hardware specifications of the BBR are summarized in Table 1. Aluminum profiles are used as the body frame to support the load and maintain its shape. The plates for placing parts in the body frame and the rim structure for holding a ball are made using a 3D printer. I design the unique robot's body to be thin and narrow to enable functional expansion for future ball-balancing robots. For example, equipment for interacting with people or cases for use in performances can be attached to the body frame.



(a)



(b)

FIGURE 4. (a) A 13S1P battery pack (rated 48.1V, charged 54.6V) for motor drivers and an interface module and (b) a 4S2P battery (rated 14.8V, charged 16.8V) for a mini PC, respectively.



FIGURE 5. An interface module (1st layer: DC-DC converter PCB, 2nd layer: microcontroller PCB, 3rd layer: IMU and connectors PCB).

III. THE MATHEMATICAL MODEL OF THE BALL-BALANCING ROBOT

The mathematical models for the ball-balancing robot (BBR) are described by dividing it into three planes. Each model has a virtual wheel that rotates the ball. Since the model for the frontal plane is the same as that for the longitudinal plane, it is not described separately. Therefore, only the models for the longitudinal plane and the horizontal plane are detailed.

A. EQUATIONS OF MOTION IN THE LONGITUDINAL PLANE

The model in the longitudinal plane is shown in Fig. 7. Regarding the body, m_B , J_{By} , L_B , and θ_y are the mass, moment of inertia, length between the center of the ball and the mass center of the body, and the orientation of the body, respectively. For the virtual wheel, m_W , J_{W_y} , r_W , and $\dot{\psi}_y$ are



FIGURE 6. The developed ball-balancing robot.

the mass, moment of inertia, radius, and angular velocity of the wheel, respectively. Finally, for the ball, m_A , J_{Ay} , r_A , x_A , and $\dot{\phi}_y$ are the mass, moment of inertia, radius, displacement, and angular velocity of the ball, respectively.

To derive the relationship with the ball and the wheel, we consider that the velocity of the ball is same as that of the wheel at c_y . First, the velocity of the ball at c_y is

$$\begin{aligned} v_{B,c_y} &= \begin{bmatrix} \dot{x}_A \\ 0 \\ 0 \end{bmatrix} + \begin{bmatrix} 0 \\ \dot{\phi}_y \\ 0 \end{bmatrix} \times \begin{bmatrix} r_A s \theta_y \\ 0 \\ r_A c \theta_y \end{bmatrix} \\ &= \begin{bmatrix} r_A \dot{\phi}_y + r_A c \theta_y \dot{\phi}_y \\ 0 \\ -r_A s \theta_y \dot{\phi}_y \end{bmatrix}. \end{aligned} \quad (5)$$

Second, the velocity of the wheel at c_y is

$$\begin{aligned} v_{W,c_y} &= \begin{bmatrix} \dot{x}_A \\ 0 \\ 0 \end{bmatrix} + \begin{bmatrix} 0 \\ \dot{\theta}_y \\ 0 \end{bmatrix} \times \begin{bmatrix} (r_A + r_W) s \theta_y \\ 0 \\ (r_A + r_W) c \theta_y \end{bmatrix} \\ &\quad + \begin{bmatrix} 0 \\ -\dot{\psi}_y \\ 0 \end{bmatrix} \times \begin{bmatrix} -r_W s \theta_y \\ 0 \\ -r_W c \theta_y \end{bmatrix} \\ &= \begin{bmatrix} r_A \dot{\phi}_y + (r_A + r_W) c \theta_y \dot{\phi}_y + r_W c \theta_y \dot{\psi}_y \\ 0 \\ -(r_A + r_W) s \theta_y \dot{\phi}_y - r_W s \theta_y \dot{\psi}_y \end{bmatrix}. \end{aligned} \quad (6)$$

TABLE 1. Hardware specifications of the ball-balancing robot.

Mass	8.9 kg
Height	0.9 m
Degrees of freedom	3
Motor	Maxon EC-i 40, 48V, 100W × 3
Speed reducer	Customized stepped planetary gear, ratio 9.035:1
Motor driver	ELMO G-SOLWHI20/100S × 3
Sensor	RENISHAW Orbis™ true, absolute rotary encoder × 3
	ANALOG DEVICES 6-axis IMU × 1
Communication	CAN 2.0A
PC	INTEL® NUC i3-1315U, 1.2GHz, RAM 32GB, SSD 256GB
OS	Ubuntu 20.04 based on a Xenomai-patched Linux kernel
Supply voltages	48.1V for motor drivers and an interface module 14.8V for PC

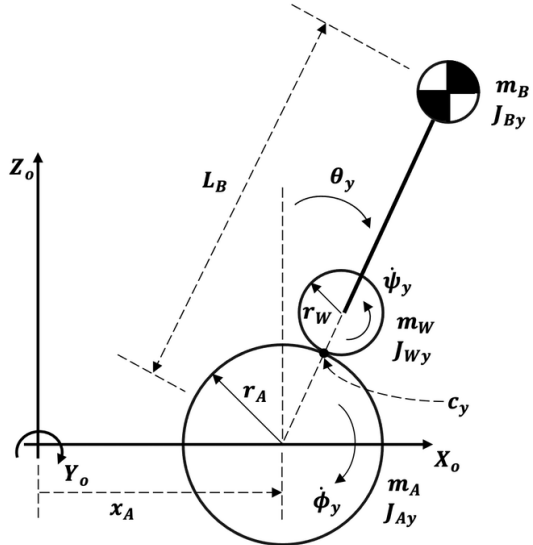


FIGURE 7. The model of the longitudinal plane.

With the no-slip condition, (5) is equal to (6). Thus,

$$r_A \dot{\phi}_y = (r_A + r_W) \dot{\theta}_y + r_W \dot{\psi}_y. \quad (7)$$

Rearranging (7), we get following.

$$\dot{\psi}_y = \frac{r_A}{r_W} (\dot{\phi}_y - \dot{\theta}_y) - \dot{\theta}_y. \quad (8)$$

To derive the equations of motion, the Lagrangian method is used. For the ball, the potential energy is $V_{Ay} = 0$, and the kinetic energy is

$$T_{Ay} = \frac{1}{2} m_A r_A^2 \dot{\phi}_y^2 + \frac{1}{2} J_{Ay} \dot{\phi}_y^2. \quad (9)$$

For the wheel, the kinetic and potential energy are as follows.

$$\begin{aligned} T_{wy} &= \frac{1}{2} m_W \left[\{r_A \dot{\phi}_y + (r_A + r_W) c \theta_y \dot{\theta}_y\}^2 \right. \\ &\quad \left. + \{(r_A + r_W) s \theta_y \dot{\theta}_y\}^2 \right] + \frac{1}{2} J_{wy} \dot{\psi}_y^2, \end{aligned} \quad (10)$$

$$V_{wy} = m_W g (r_A + r_W) c \theta_y. \quad (11)$$

Substituting (8) into (10) and then simplifying (10) yields

$$\begin{aligned} T_{wy} = & \frac{1}{2}m_W \left\{ r_A^2 \dot{\phi}_y^2 + (r_A + r_W)^2 \dot{\theta}_y^2 \right. \\ & \left. + 2r_A(r_A + r_W)c\theta_y \dot{\theta}_y \dot{\phi}_y \right\} \\ & + \frac{1}{2}J_{WY} \left\{ \frac{r_A}{r_W}(\dot{\phi}_y - \dot{\theta}_y) - \dot{\theta}_y \right\}^2. \end{aligned} \quad (12)$$

For the body, the kinetic and potential energy are as follows.

$$\begin{aligned} T_{By} = & \frac{1}{2}m_B \left(r_A^2 \dot{\phi}_y^2 + L_B^2 \dot{\theta}_y^2 \right. \\ & \left. + 2r_A L_B c\theta_y \dot{\theta}_y \dot{\phi}_y \right) + \frac{1}{2}J_{By} \dot{\theta}_y^2, \end{aligned} \quad (13)$$

$$V_{By} = m_B g L_B c\theta_y. \quad (14)$$

Thus, the total kinetic energy is $T_y = T_{Ay} + T_{Wy} + T_{By}$, and the total potential energy is $V_y = V_{Ay} + V_{Wy} + V_{By}$.

Define the generalized coordinates $q_y = [\phi_y \ \theta_y]^T$. The Lagrangian is defined to be $L(q_y, \dot{q}_y) = T_y - V_y$. The Euler-Lagrange equations of motion in the longitudinal plane are

$$\frac{d}{dt} \frac{\partial L}{\partial \dot{q}_y} - \frac{\partial L}{\partial q_y} = \begin{bmatrix} r_A/r_W \\ -r_A/r_W \end{bmatrix} \tau_y \quad (15)$$

After calculating the derivatives in the Euler-Lagrange equations and reorganizing the terms, the equations of motion can be expressed as follows.

$$M(q_y) \ddot{q}_y + C(q, \dot{q}_y) + G(q) = \begin{bmatrix} r_A/r_W \\ -r_A/r_W \end{bmatrix} \tau_y, \quad (16)$$

where τ_y is the torque of the virtual wheel. The mass matrix, $M(q_y)$, is

$$M(q_y) = \begin{bmatrix} M_{y,11} & M_{y,12} \\ M_{y,12} & M_{y,22} \end{bmatrix}$$

where

$$\begin{aligned} M_{y,11} = & (m_A + m_W + m_B)r_A^2 + J_{Ay} + J_{Wy} \frac{r_A^2}{r_W^2} \\ M_{y,12} = & \{m_W(r_A + r_W) + m_B L_B\} r_A c\theta_y \\ & - J_{Wy} \frac{r_A}{r_W} \left(\frac{r_A}{r_W} + 1 \right) \\ M_{y,22} = & m_W(r_A + r_W)^2 + m_B L_B^2 + J_{By} \\ & + J_{Wy} \left(\frac{r_A}{r_W} + 1 \right)^2. \end{aligned}$$

The vector of Coriolis and centrifugal force, $C(q, \dot{q}_y)$, and the vector of gravitational force, $G(q)$, are

$$C(q, \dot{q}_y) = \begin{bmatrix} -\{m_W(r_A + r_W) + m_B L_B\} r_A s\theta_y \dot{\theta}_y^2 \\ 0 \end{bmatrix},$$

and

$$G(q) = \begin{bmatrix} 0 \\ -\{m_W(r_A + r_W) + m_B L_B\} g s\theta_y \end{bmatrix},$$

respectively.

B. EQUATIONS OF MOTION IN THE HORIZONTAL PLANE

The model in the horizontal plane is shown in Fig. 8. (a). The notation rules for the horizontal plane are the same as those for the longitudinal plane. In the model of the horizontal plane, the α is the angle from the vertical axis of the body to the point where the ball and the wheel meet and is shown in Fig. 8. (b).

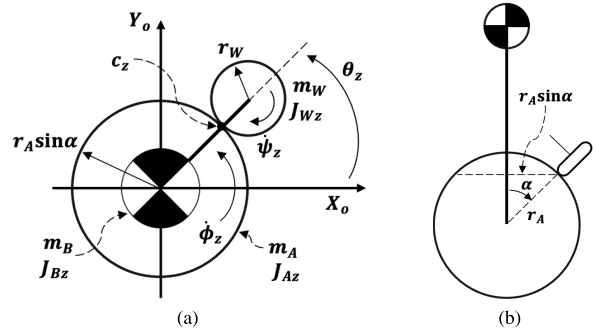


FIGURE 8. (a) The model of the horizontal plane. (b) The α is the zenith angle of the wheel.

The relationship with the ball and the wheel is derived from the condition that the velocities at c_z are equal. Thus,

$$r_A s\alpha \dot{\phi}_z = (r_A s\alpha + r_W) \dot{\theta}_z + r_W \dot{\psi}_z \quad (17)$$

Rearranging (17), we get following.

$$\dot{\psi}_z = \frac{r_A s\alpha}{r_W} (\dot{\phi}_z - \dot{\theta}_z) - \dot{\theta}_z \quad (18)$$

The total potential energy in the horizontal plane is $V_z = 0$, and the total kinetic energy is as follows.

$$T_z = \frac{1}{2}J_{Az}\dot{\phi}_z^2 + \frac{1}{2}J_{Wz} \left\{ \frac{r_A s\alpha}{r_W} (\dot{\phi}_z - \dot{\theta}_z) - \dot{\theta}_z \right\}^2 + \frac{1}{2}J_{Bz}\dot{\theta}_z^2 \quad (19)$$

Define the generalized coordinates $q_z = [\phi_z \ \theta_z]^T$. The Lagrangian is defined to be $L(q_z, \dot{q}_z) = T_z$. From the Euler-Lagrange equations, the equations of motion in the horizontal plane is derived as follows.

$$M(q_z) \ddot{q}_z = \begin{bmatrix} \frac{r_A s\alpha}{r_W} \tau_z - \tau_f \\ -\frac{r_A s\alpha}{r_W} \tau_z \end{bmatrix}, \quad (20)$$

where τ_z and τ_f are the torque of the virtual wheel and the friction torque between the ball and the ground, respectively. The mass matrix, $M(q_z)$, is

$$M(q_z) = \begin{bmatrix} M_{z,11} & M_{z,12} \\ M_{z,12} & M_{z,22} \end{bmatrix}$$

where

$$\begin{aligned} M_{z,11} = & J_{Az} + J_{Wz} \frac{r_A^2 s^2 \alpha}{r_W^2} \\ M_{z,12} = & - \left(1 + \frac{r_W}{r_A s\alpha} \right) J_{Wz} \frac{r_A^2 s^2 \alpha}{r_W^2} \\ M_{z,22} = & J_{Bz} + \left(1 + \frac{r_W}{r_A s\alpha} \right)^2 J_{Wz} \frac{r_A^2 s^2 \alpha}{r_W^2}. \end{aligned}$$

From the no-rotation condition of the ball against the ground, $\ddot{\phi}_z = 0$, then (20) can be simplified as follows.

$$\ddot{\theta}_z = C_z \tau_z, \quad (21)$$

where

$$C_z = -\frac{r_A r_W s\alpha}{J_{Wz} r_A^2 s^2 \alpha + (J_{Bz} + J_{Wz}) r_W^2 + 2 J_{Wz} r_A r_W s\alpha}.$$

C. TORQUE CONVERSION

The torques on the virtual wheels have to be converted into the torques for the real omniwheels. To derive the relationship between the virtual and real ones, we use the property that the sum of the torques acting on the ball is the same in both the virtual and real models. The diagram of each model is shown in Fig. 9.

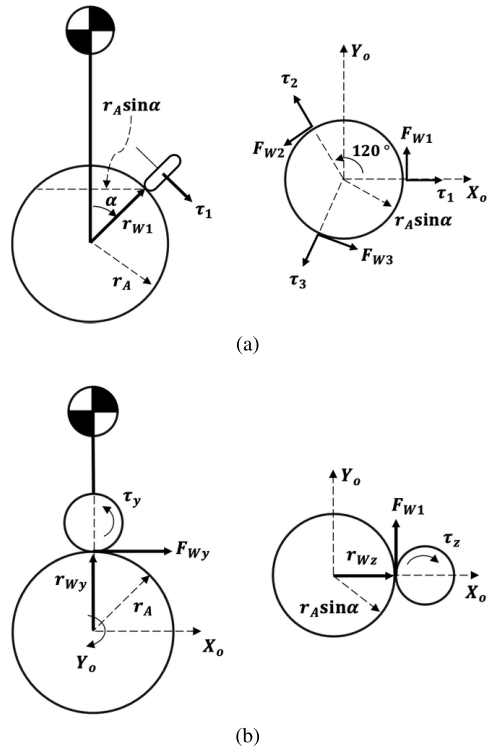


FIGURE 9. (a) The diagram of the torques, tangential forces and moment arms of the three omniwheels. (b) The diagram of the torques, tangential forces and moment arms of the virtual wheels in the longitudinal and horizontal planes, respectively.

First, referring to Fig. 9. (a), the tangential forces exerted by the real omniwheels on the ball and moment arms are

$$F_{W1} = \frac{\tau_1}{r_W} \begin{bmatrix} 0 \\ 1 \\ 0 \end{bmatrix}, F_{W2} = \frac{\tau_2}{r_W} \begin{bmatrix} -\frac{\sqrt{3}}{2} \\ 0 \\ -\frac{1}{2} \end{bmatrix},$$

$$F_{W3} = \frac{\tau_3}{r_W} \begin{bmatrix} \frac{\sqrt{3}}{2} \\ -\frac{1}{2} \\ 0 \end{bmatrix},$$

$$r_{W1} = \begin{bmatrix} r_A s\alpha \\ 0 \\ r_A c\alpha \end{bmatrix}, r_{W2} = \begin{bmatrix} -\frac{1}{2} r_A s\alpha \\ \frac{\sqrt{3}}{2} r_A s\alpha \\ r_A c\alpha \end{bmatrix},$$

$$r_{W3} = \begin{bmatrix} -\frac{1}{2} r_A s\alpha \\ -\frac{\sqrt{3}}{2} r_A s\alpha \\ r_A c\alpha \end{bmatrix}.$$

The torques are $T_i = r_{Wi} \times F_{Wi}$ ($i = 1, 2, 3$), and the sum of the torques is

$$T_{OW} = T_1 + T_2 + T_3 = \frac{r_A \tau_1}{r_W} \begin{bmatrix} -c\alpha \\ 0 \\ s\alpha \end{bmatrix} + \frac{r_A \tau_2}{r_W} \begin{bmatrix} \frac{1}{2} c\alpha \\ -\frac{\sqrt{3}}{2} c\alpha \\ s\alpha \end{bmatrix} + \frac{r_A \tau_3}{r_W} \begin{bmatrix} \frac{1}{2} c\alpha \\ \frac{\sqrt{3}}{2} c\alpha \\ s\alpha \end{bmatrix}. \quad (22)$$

Second, referring to Fig. 9. (b), the tangential forces exerted by the virtual wheels on the ball and moment arms are

$$F_{Wx} = \frac{\tau_x}{r_W} \begin{bmatrix} 0 \\ 1 \\ 0 \end{bmatrix}, F_{Wy} = \frac{\tau_y}{r_W} \begin{bmatrix} 1 \\ 0 \\ 0 \end{bmatrix}, F_{Wz} = \frac{\tau_z}{r_W} \begin{bmatrix} 0 \\ 0 \\ 1 \end{bmatrix},$$

$$r_{Wx} = \begin{bmatrix} 0 \\ 0 \\ r_A \end{bmatrix}, r_{Wy} = \begin{bmatrix} 0 \\ 0 \\ r_A \end{bmatrix}, r_{Wz} = \begin{bmatrix} r_A s\alpha \\ 0 \\ 0 \end{bmatrix}.$$

The torques are $T_i = r_{Wi} \times F_{Wi}$ ($i = x, y, z$), and the sum of the torques is

$$T_{VW} = T_x + T_y + T_z = \frac{r_A \tau_x}{r_W} \begin{bmatrix} -1 \\ 0 \\ 0 \end{bmatrix} + \frac{r_A \tau_y}{r_W} \begin{bmatrix} 0 \\ 1 \\ 0 \end{bmatrix} + \frac{r_A s\alpha \tau_z}{r_W} \begin{bmatrix} 0 \\ 0 \\ 1 \end{bmatrix}. \quad (23)$$

Thus, from the torque conservation, (22) is equal to (23),

$$T_{OW} = T_{VW}. \quad (24)$$

Rearranging (24), the relationship between the virtual torques and the real ones can be represented in matrix form as follows.

$$\begin{bmatrix} \tau_1 \\ \tau_2 \\ \tau_3 \end{bmatrix} = \begin{bmatrix} \frac{2}{3c\alpha} & 0 & \frac{1}{3} \\ -\frac{1}{3c\alpha} & -\frac{\sqrt{3}}{3c\alpha} & \frac{1}{3} \\ -\frac{1}{3c\alpha} & \frac{\sqrt{3}}{3c\alpha} & \frac{1}{3} \end{bmatrix} \begin{bmatrix} \tau_x \\ \tau_y \\ \tau_z \end{bmatrix}. \quad (25)$$

IV. BALANCING CONTROL SCHEME

A ball-balancing robot (BBR) must inherently maintain its posture upright, necessitating balancing control. Since the equilibrium point of the BBR is the upright position, the equations of motion in the longitudinal plane, (16), can be linearized at that point. If the state vector is defined as $X_y = [\phi_y \theta_y \dot{\phi}_y \dot{\theta}_y]^T$, the equilibrium point is $X_y = 0$. Linearizing (16) is

$$\begin{bmatrix} \ddot{\phi}_y \\ \ddot{\theta}_y \end{bmatrix} = M_L^{-1} \left\{ -G_L + \begin{bmatrix} r_A/r_W \\ -r_A/r_W \end{bmatrix} \tau_y \right\}. \quad (26)$$

Assume that

$$M_L^{-1} = \begin{bmatrix} \mu_1 & \mu_2 \\ \mu_3 & \mu_4 \end{bmatrix}, \quad (27)$$

where $\mu_i (i = 1, 2, 3, 4)$ is each element of the inverse matrix of the linearized mass matrix, (26) is expressed in the state-space form as follows.

$$\begin{bmatrix} \dot{\phi}_y \\ \dot{\theta}_y \\ \ddot{\phi}_y \\ \ddot{\theta}_y \end{bmatrix} = \begin{bmatrix} 0 & 0 & 1 & 0 \\ 0 & 0 & 0 & 1 \\ 0 & \mu_2 \{m_W(r_A + r_W) - m_B L_B\} g & 0 & 0 \\ 0 & \mu_4 \{m_W(r_A + r_W) - m_B L_B\} g & 0 & 0 \end{bmatrix} \\ \times \begin{bmatrix} \phi_y \\ \theta_y \\ \dot{\phi}_y \\ \dot{\theta}_y \end{bmatrix} + \begin{bmatrix} 0 \\ 0 \\ \frac{r_A}{r_W}(\mu_1 - \mu_2) \\ \frac{r_A}{r_W}(\mu_3 - \mu_4) \end{bmatrix} \tau_y. \quad (28)$$

In case of the horizontal plane, define the state vector as $X_z = [\theta_z \dot{\theta}_z]^T$. Equation (21) is expressed in the state-space form as follows.

$$\begin{bmatrix} \dot{\theta}_z \\ \ddot{\theta}_z \end{bmatrix} = \begin{bmatrix} 0 & 1 \\ 0 & 0 \end{bmatrix} \begin{bmatrix} \theta_z \\ \dot{\theta}_z \end{bmatrix} + \begin{bmatrix} 0 \\ C_z \end{bmatrix} \tau_z \quad (29)$$

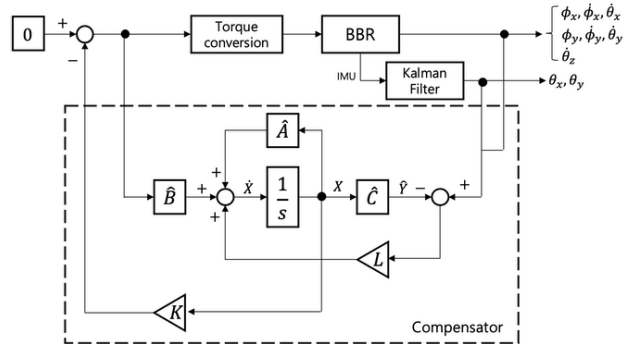


FIGURE 10. A schematic of the compensator for balancing control.

For balancing control, the compensator shown in Fig. 10 is applied. The compensator consists of a closed-loop observer and full-state feedback, and it works to keep the states at zero. The matrix \hat{A} and vector \hat{B} of the closed-loop observer are determined from (28) and (29). Also, the matrix \hat{C} is the identity matrix. The observer receives two inputs: wheel torques and measured states. It adjusts the model states through the state errors to reduce the modeling error. To measure the states of the BBR, including the angles and angular velocity of the body posture and those of the ball, the IMU and encoder data are used. Specifically, the angles of the body posture, except for the yaw angle, are estimated through a Kalman Filter using IMU data because the IMU is not integrated with a magnetometer.

V. EXPERIMENTAL RESULTS

An experiment is conducted to verify whether the developed ball-balancing robot (BBR) can maintain an upright position using the applied balancing controller. In Fig. 11, the balancing experiment is shown, illustrating the robot's ability to maintain equilibrium. The blue dashed line serves as a reference for the upright position. The robot moved backward slightly to maintain its balance from Fig. 11. (1) to (5), but it

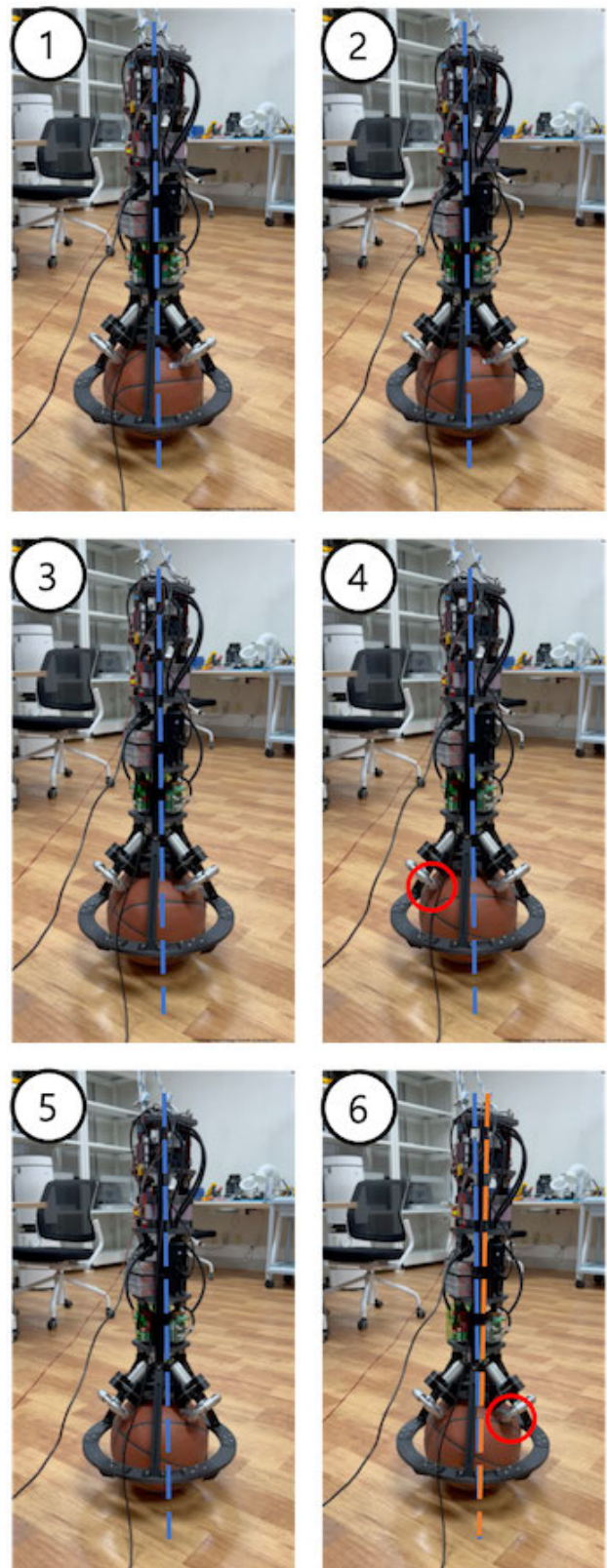


FIGURE 11. The snapshots of the balancing experiment.

started to fall from (6). The orange dashed line of the (6), compared to the reference line, shows the robot is tilted to

the right. It managed to keep its balance for approximately 6 seconds, and the resulting graph is shown below.

The pitch and roll angular velocities of the body are presented in Fig. 12 and 13, respectively. The measured angular velocities from the IMU are represented by blue lines, while the estimated ones from the observer are shown as orange lines. Both the measured and estimated data are closely aligned and maintained near zero, indicating that the compensator is effectively maintaining the robot's balance in the pitch and roll directions. The close match between the observed and measured data confirms the accuracy and reliability of the observer. The pitch and roll angle of the body are presented in Fig. 14 and 15, respectively. Additionally, the measured angles calculated by the Kalman Filter are represented by blue lines, while the estimated ones from the observer are shown as orange lines. The angles are also maintained near zero, which indicates effective balance control in the roll direction, similar to the pitch direction.

In Fig. 12, 13, 14, and 15, there are relatively large fluctuations in angular velocity and angle around 4 seconds. Next, In Fig. 14, and 15, the angles diverge around 6 seconds. The cause will be examined in the next section.

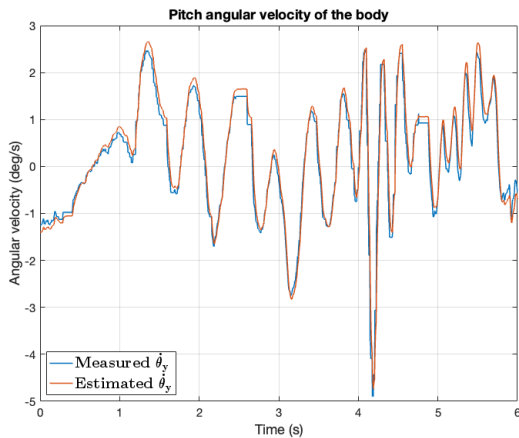


FIGURE 12. The pitch angular velocity of the body.

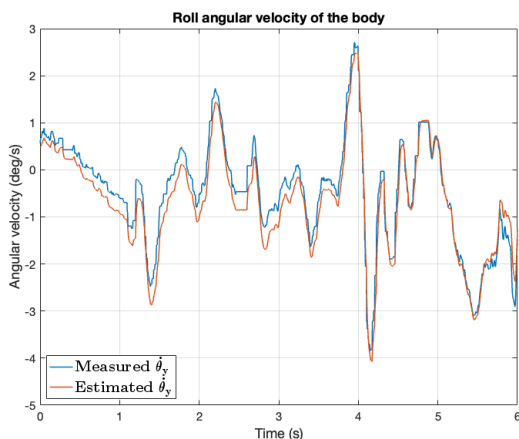


FIGURE 13. The roll angular velocity of the body.

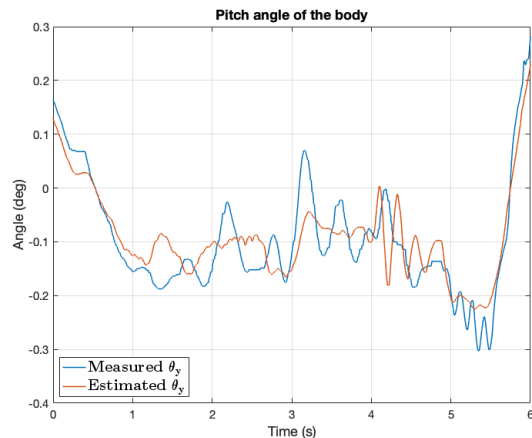


FIGURE 14. The pitch angle of the body.

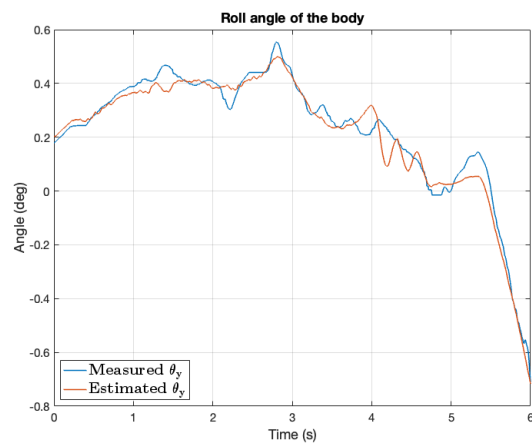


FIGURE 15. The roll angle of the body.

VI. DISCUSSION

Although a balancing control experiment was conducted, the ball-balancing robot (BBR) was not able to maintain its posture for a sufficient amount of time. This issue is caused by vibrations occurring when the omniwheels pass over the grooves of a basketball. Fig. 11 (4) and (6) shows that the left omniwheel of the BBR crosses the groove of the basketball, and the right one crosses the groove of the basketball, respectively. At that moment, the vibration acts as a disturbance to the robot. Therefore, it appears necessary to design a customized smoother ball or to use a bowling ball instead of a basketball and to apply an additional controller to eliminate disturbances.

VII. CONCLUSION

The ball-balancing robot (BBR) designed in this study represents a significant advancement in robotics, particularly in terms of its unique thin and narrow body design, customized stepped planetary gear, and the implementation of a compensator with an observer and full-state feedback. The experimental results have shown that while the BBR

can effectively balance, it faces challenges such as vibrations caused by the omniwheels passing over the grooves of a basketball. To address this, future iterations should consider designing a smoother ball and incorporating additional controllers to eliminate disturbances. Additionally, a LiDAR (Light Detection and Ranging) will be attached on top of the BBR for autonomous movements, and speakers and LEDs will be installed on the sides for entertainment. Despite these challenges, the innovative design and control strategies developed in this study lay a solid foundation for the future development of more stable and efficient ball-balancing robots. These advancements will enhance the robot's applicability in dynamic environments, making it a valuable tool for various service and entertainment applications.

REFERENCES

- [1] T. B. Lauwers, G. A. Kantor, and R. L. Hollis, "A dynamically stable single-wheeled mobile robot with inverse mouse-ball drive," in *Proc. IEEE Int. Conf. Robot. Autom. (ICRA)*, May 2006, pp. 2884–2889.
- [2] U. Nagarajan, G. Kantor, and R. Hollis, "The ballbot: An omnidirectional balancing mobile robot," *Int. J. Robot. Res.*, vol. 33, no. 6, pp. 917–930, May 2014.
- [3] U. Nagarajan and R. Hollis, "Shape space planner for shape-accelerated balancing mobile robots," *Int. J. Robot. Res.*, vol. 32, no. 11, pp. 1323–1341, Sep. 2013.
- [4] G. Seyfarth, A. Bhatia, O. Sassenick, M. Shomin, M. Kumagai, and R. Hollis, "Initial results for a ballbot driven with a spherical induction motor," in *Proc. IEEE Int. Conf. Robot. Autom. (ICRA)*, May 2016, pp. 3771–3776.
- [5] M. Kumagai and T. Ochiai, "Development of a robot balancing on a ball," in *Proc. Int. Conf. Control. Autom. Syst.*, Oct. 2008, pp. 433–438.
- [6] M. Kumaga and T. Ochiai, "Development of a robot balanced on a ball—Application of passive motion to transport," in *Proc. IEEE Int. Conf. Robot. Autom.*, May 2009, pp. 4106–4111.
- [7] L. Hertig, D. Schindler, M. Bloesch, C. D. Remy, and R. Siegwart, "Unified state estimation for a ballbot," in *Proc. IEEE Int. Conf. Robot. Autom.*, May 2013, pp. 2471–2476.
- [8] D. Pham, H. Kim, J. Kim, and S. Lee, "Balancing and transferring control of a ball segway using a double-loop approach," *IEEE Control Syst.*, vol. 38, no. 2, pp. 15–37, Jul. 2018.
- [9] D. B. Pham, X. Q. Duong, D. S. Nguyen, M. C. Hoang, D. Phan, E. Asadi, and H. Khayyam, "Balancing and tracking control of ballbot mobile robots using a novel synchronization controller along with online system identification," *IEEE Trans. Ind. Electron.*, vol. 70, no. 1, pp. 657–668, Jan. 2023.
- [10] J. Jo and Y. Oh, "Contact force based balancing and tracking control of a ballbot using projected task space dynamics with inequality constraints," in *Proc. 17th Int. Conf. Ubiquitous Robots (UR)*, Jun. 2020, pp. 118–123.
- [11] S.-M. Lee and B. S. Park, "Robust control for trajectory tracking and balancing of a ballbot," *IEEE Access*, vol. 8, pp. 159324–159330, 2020.
- [12] C. Xiao, M. Mansouri, D. Lam, J. Ramos, and E. T. Hsiao-Wecksler, "Design and control of a ballbot drivetrain with high agility, minimal footprint, and high payload," in *Proc. IEEE/RSJ Int. Conf. Intell. Robots Syst. (IROS)*, vol. 32, Oct. 2023, pp. 376–383.
- [13] H. Jang, C. Hyun, and B. S. Park, "Virtual angle-based adaptive control for trajectory tracking and balancing of ball-balancing robots without velocity measurements," *Int. J. Adapt. Control Signal Process.*, vol. 37, no. 8, pp. 2204–2215, Aug. 2023.
- [14] P. Fankhauser and C. Gwerder, "Modeling and control of a ballbot," BA thesis, Dept. Mech. Process Eng., ETH, Zurich, Switzerland, 2010.
- [15] I. Lal, M. Nicoara, A. Codrean, and L. Busoni, "Hardware and control design of a ball balancing robot," in *Proc. IEEE 22nd Int. Symp. Design Diag. Electron. Circuits Syst. (DDECS)*, Apr. 2019, pp. 1–6.
- [16] A. N. Inal, Ö. Morgül, and U. Saranlı, "A 3D dynamic model of a spherical wheeled self-balancing robot," in *Proc. IEEE/RSJ Int. Conf. Intell. Robots Syst.*, Oct. 2012, pp. 5381–5386.
- [17] T. Endo and Y. Nakamura, "An omnidirectional vehicle on a basketball," in *Proc. 12th Int. Conf. Adv. Robot. (ICAR)*, 2005, pp. 573–578.



SANGSIN PARK received the B.S. degree in mechanical engineering from Inha University, Incheon, South Korea, in 2005, and the M.S. and Ph.D. degrees in mechanical engineering from Korea Advanced Institute of Science and Technology (KAIST), Daejeon, South Korea, in 2007 and 2017, respectively.

He was a Postdoctoral Researcher with the Department of Mechanical Engineering, University of Nevada, Las Vegas, from 2017 to 2019, a Principal Researcher with Rainbow Robotics, Daejeon, in 2019, and the Team Leader of Gentle Monster, Seoul, South Korea. Since 2022, he has been an Assistant Professor with the Mechanical Engineering Department, Korea National University of Transportation (KNUT), Chungju-si, South Korea. His research interests include robot mechanism design, robot system integration, real-world application, and legged robots.